





On the Nucleosynthesis in Accretion-Induced Collapse of White Dwarfs

CHUN-MING YIP ¹, MING-CHUNG CHU ¹, SHING-CHI LEUNG ² AND LAP-MING LIN ¹

¹*Department of Physics and Institute of Theoretical Physics, The Chinese University of Hong Kong, Shatin, N.T., Hong Kong S.A.R., People's Republic of China*

²*Department of Mathematics and Physics, SUNY Polytechnic Institute, 100 Seymour Road, Utica, NY 13502, USA*

Submitted to ApJ

ABSTRACT

It has long been hypothesized that accretion-induced collapse (AIC) of white dwarfs contribute to heavy chemical elements production in the universe. We present one-dimensional neutrino-radiative hydrodynamic simulations of AIC followed by post-processing nucleosynthesis calculations of the ejecta. A proto-neutron star is formed after the AIC, and a neutrino burst with peak luminosity $\sim 10^{53}$ erg s⁻¹, comparable to that of a core-collapse supernova (CCSN), is emitted. The ejecta mass of AIC could be up to $\sim 10^{-2} M_{\odot}$, and the first neutron-capture peak elements (Sr, Y, and Zr) could be abundantly synthesized, with an overproduction of $\sim 10^6$ relative to the solar abundances. The yield of ⁵⁶Ni could be up to at most $\sim 10^{-3} M_{\odot}$, suggesting that the electromagnetic light curve associated with AIC is at least 2 orders dimmer than those associated with Type Ia supernovae (Type Ia SN). The inferred upper bound of AIC event rate, from nucleosynthesis calculations, is at most $\sim 10\%$ relative to those of CCSNe and Type Ia SNe.

Keywords: Astronomical simulations (1857) — Hydrodynamical simulations (767) — Supernova neutrinos (1666) — Supernova remnants (1667) — Nucleosynthesis (1131) — Solar abundances (1474)

1. INTRODUCTION

1.1. *Accretion-induced Collapse of White Dwarfs*

A typical carbon-oxygen white dwarf (WD) explodes as a Type Ia supernova (Type Ia SN) when it approaches the Chandrasekhar limit through mass accretion. Nomoto & Kondo (1991), on the other hand, proposed that electron capture could be triggered at the core of an oxygen-neon-magnesium WD and reduce the electron degeneracy pressure above certain threshold densities. In this scenario, the WD would undergo gravitational collapse, thus called accretion-induced collapse (AIC), to form a proto-neutron star (PNS) rather than a thermonuclear explosion that results in a Type Ia SN. Several studies revisited the AIC with oxygen-neon WDs being the progenitors (Wu & Wang 2018; Wang 2018; Ruiter et al. 2019). A recent work by Mori et al. (2023) also discusses the initial conditions of super-Chandrasekhar AIC progenitors. A similar electron capture mechanism was also employed to account for the gravitational collapse and explosion for super-asymptotic giant branch (AGB) stars of 8 – 10 M_{\odot} as electron-capture supernovae (ECSNe) (Leung & Nomoto 2019; Leung et al. 2020).

Neutron stars follow a bimodal mass distribution (e.g., (Schwab et al. 2010; Farrow et al. 2019)). AIC is a possible formation channel of the low-mass neutron stars since

the AIC progenitor mass does not exceed the Chandrasekhar limit. Moreover, it was proposed that AIC could be an explanation of multi-wavelength electromagnetic (EM) transients, including fast radio burst (Piro & Kulkarni 2013; Moriya 2016; Margalit et al. 2019), X-ray transient (Yu et al. 2019), and gamma-ray burst (Yi & Blackman 1998). Nevertheless, these transients are known to be faint and short-lived due to the low yield of ⁵⁶Ni up to at most $\sim 10^{-2} M_{\odot}$ (Metzger et al. 2009). Although there is no confirmed EM observation of AIC yet, such an event may be alternatively identified through multi-messenger observations. The axisymmetric general relativistic simulations of AIC by Abdikamalov et al. (2010) predicted that the gravitational-wave signal of a galactic AIC event would be detectable. Multidimensional simulations of AIC with neutrino transport were also performed by Dessart et al. (2006, 2007) to study the effects of neutrino-matter interactions on explosion dynamics. A recent work on three-dimensional general relativistic simulations with neutrino transport by Micchi et al. (2023) reported that the neutrino burst associated with AIC is as bright as those emitted by core-collapse supernovae (CCSNe). The next generation of neutrino detectors, such as JUNO (Yang & JUNO Collaboration 2022) and DUNE (Falcone & DUNE Collaboration 2022), may help identify AICs. The upcoming

multi-messenger observations offer excellent opportunities to study AIC with unprecedented details.

1.2. Supernova Nucleosynthesis

It is widely believed that about half of the heavy chemical elements in nature are produced by astrophysical rapid neutron-capture process (r -process) nucleosynthesis (see the reviews by e.g., [Kajino et al. \(2019\)](#); [Cowan et al. \(2021\)](#)). AIC was hypothesized to be a promising r -process nucleosynthesis site for its neutron-rich outflow ([Woosley & Baron 1992](#); [Fryer et al. 1999](#)). The event rate of AICs, accordingly, could be inferred from its production curves. The study by [Darbha et al. \(2010\)](#) determined that the first neutron-capture peak elements (Sr, Y, and Zr) could be synthesized through AIC, and the event rate of AICs is predicted to be $\sim 10^{-2}$ of the event rate of Type Ia SNe. Without taking AIC into account, the review by [Kobayashi et al. \(2020a\)](#) argued that the first neutron-capture peak elements are sufficiently produced by ECSNe and AGB stars. The calculations by [Wanajo et al. \(2009, 2011\)](#) deduced the overproduction of the first neutron-capture peak elements through an ECSN event, and hence imposed a constraint on the event rate of ECSNe relative to other CCSNe.

In this paper, we perform one-dimensional hydrodynamic simulations of AIC with neutrino transport to investigate the properties of its mass outflow, as well as post-processing nucleosynthesis calculations to study its chemical elements production. In addition, we investigate the equation of state (EoS) dependence of ejecta properties and characteristic isotopes production of AIC. In the following discussion, we show that AIC may significantly contribute to the production of the first neutron-capture peak elements in nature based on the production curve. Based on our results, we derive a new constraint on the event rate of AICs relative to Type Ia SNe and CCSNe from our nucleosynthesis calculations. Due to the degeneracy of production patterns between AICs and ECSNe, the former constraints on the event rate of ECSNe suggested by [Wanajo et al. \(2009, 2011\)](#) may also be affected after including the contribution from AICs.

This paper is organized as follows. In Section 2, we introduce the computational setup of the neutrino radiation hydrodynamic simulations and nucleosynthesis calculations used. The numerical results of the simulations and calculations are presented in Section 3. We summarize and discuss the implications of these results in Section 4 followed by our conclusions in Section 5.

2. METHODOLOGY

2.1. Initial Models

We construct spherically symmetric WD models as AIC progenitors at Newtonian hydrostatic equilibrium. An initial parameterized temperature profile is assigned to the WD

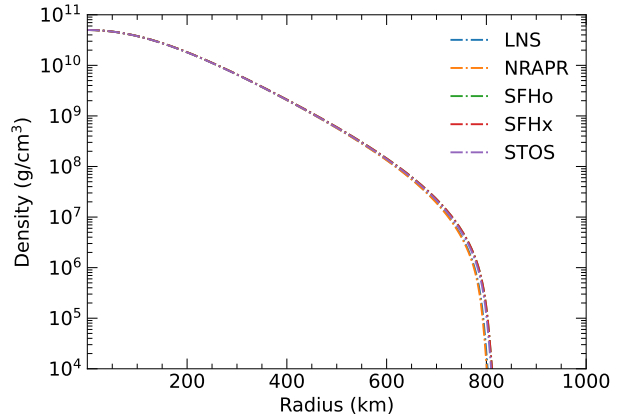


Figure 1. Density vs. radius of initial WD models using different EoSs.

models following [Dessart et al. \(2006\)](#):

$$T(\rho) = T_c \left(\frac{\rho}{\rho_c} \right)^{0.35}, \quad (1)$$

where $T_c = 10$ GK and $\rho_c = 5 \times 10^{10}$ g cm $^{-3}$ are the central temperature and density of the WDs, respectively. We employ a grid setup to define the spatial resolution r_j of the j -th grid, similar to that proposed by [Skinner et al. \(2016\)](#):

$$r_j = A_f x_t \sinh \left(\frac{j}{x_t} \right). \quad (2)$$

We set $A_f = 300$ m to be the finest resolution at the centre and $x_t = 500$, so that the progenitors are contained by about 1, 200 grids. The density profile of the initial models is shown in Figure 1. With the given T_c and ρ_c , these WDs have masses $\approx 1.4 M_\odot$ and radii ≈ 800 km that are insensitive to the EoS choice (see Section 2.3 for more details).

2.2. Hydrodynamics

In this paper, the hydrodynamic simulations of AIC are performed using the one-dimensional Newtonian hydrodynamics code developed by [Leung et al. \(2015\)](#). To mimic the general relativistic effects on the PNS with a very high compactness, we implement an effective relativistic potential and the lapse function to the Newtonian hydrodynamics following the Case A formalism in [Marek et al. \(2006\)](#) (see also [Zha et al. 2020](#), for the reference).

For the electron capture that is responsible for the gravitational collapse of the progenitors, we follow the parameterized fitting formula suggested by [Liebendörfer \(2005\)](#) to determine the electron fraction Y_e as a function of density ρ

before core bounce:

$$Y_e(x) = \frac{1}{2}(Y_1 + Y_2) + \frac{x}{2}(Y_1 - Y_2) + Y_3 \left[1 - |x| + \frac{4|x| \left(|x| - \frac{1}{2} \right)}{|x| - 1} \right], \quad (3)$$

$$x(\rho) = \max \left[-1, \min \left(1, \frac{2 \log \rho - \log \rho_2 - \log \rho_1}{\log \rho_2 - \log \rho_1} \right) \right]. \quad (4)$$

The fitting parameters ρ_1 , ρ_2 , Y_1 , Y_2 , and Y_3 are obtained from more sophisticated calculations, and they are used in several earlier simulations of AIC (Leung et al. 2019; Zha et al. 2019; Chan et al. 2023). This parameterized fitting formula for electron capture is applied until the core bounce condition is satisfied when the entropy of the core exceeds $3k_B$, where k_B is the Boltzmann constant. Neutrino pressure is included in the neutrino trapping regime at $\rho \geq 2 \times 10^{12} \text{ g cm}^{-3}$. After the core bounce, we activate a neutron transport scheme (see Section 2.4) that couples with the hydrodynamics.

In each model, we execute the hydrodynamic simulations up to 1 s after the core bounce in order to determine the mass outflow properties of AIC.

2.3. Equation of state

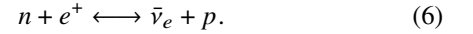
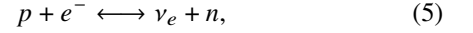
In an AIC simulation, a PNS with maximum temperature $> 10 \text{ MeV}$ and density $> 10^{14} \text{ g cm}^{-3}$ forms through the gravitational collapse of the WD. Meanwhile, the electron fraction of the PNS could drop below 0.1 as a consequence of neutronization. The properties of hot and dense nuclear matter with large isospin asymmetry are highly uncertain. The EoSs constructed for supernova simulations rely on theoretical predictions of nuclear matter properties under these extreme conditions that cannot be achieved experimentally. We adopt a few open-source EoS tables¹ to investigate the effects of varying EoS on our numerical calculations. We employ the LNS and NRAPR EoSs (Schneider et al. 2017, 2019; Cao et al. 2006; Steiner et al. 2005; Lattimer & Douglas Swesty 1991) as representative low stiffness models. For intermediate stiffness models, we choose the SFHo and SFHx EoS (Hempel & Schaffner-Bielich 2010; Steiner et al. 2013; Möller et al. 1997; Hempel et al. 2012). The STOS EoS (Shen et al. 1998, 2011) is additionally used as a high stiffness model. The incompressibility K and TOV limit M_{TOV} of these models are listed in Table 1.

2.4. Neutrino transport

Neutrinos are produced, absorbed, and scattered by matter after a PNS forms. The heating and cooling of the star

due to neutrino-matter interactions are coupled with the hydrodynamics and influence the evolution of the star. During the post-bounce phase, we evaluate the neutrino transport using the isotropic diffusion source approximation (IDSA) (Liebendörfer et al. 2009; Berninger et al. 2013).

The charged-current interactions between the electron-type neutrinos, namely ν_e and $\bar{\nu}_e$, and nucleons (neutron n and proton p) are included as the major electron-type neutrinos production and absorption channels:



Besides, the elastic scattering channels between electron-type neutrinos and nucleons, alpha particles, and nuclei are included. To include the neutrino cooling effect through heavy flavor neutrinos ν_X emissions, we adopt the leakage scheme (Rosswog & Liebendörfer 2003) for muon- and tau-type neutrinos together with a fitting formula for their pair-production rates (Itoh et al. 1996).

2.5. Nucleosynthesis

In order to investigate the chemical elements production of AIC ejecta, we use the open-source code `torch` for nuclear reaction network calculation developed by Timmes et al. (2000). The network consists of about 1,200 isotopes from neutron and proton to Sn (atomic number $Z = 50$). The nuclear masses, partition functions, and thermonuclear reaction rates, including (n, γ) , (n, p) , (p, γ) , (α, n) , (α, p) , (α, γ) , and their inverse processes, are obtained from Cyburt et al. (2010). The weak decay rates of isotopes computed by Möller et al. (2003) are used². Some special nuclear reactions, such as triple-alpha process, are also attached to the network.

We perform the post-processing nucleosynthesis calculations by mapping the hydrodynamic and thermodynamic quantities of the ejected material, obtained from the hydrodynamic simulations of AIC done in Section 2.2, to about 30 trajectories. After that, we evaluate the nucleosynthesis of these trajectories by solving the nuclear reaction network explicitly. We start the nucleosynthesis calculations when the temperature of the ejecta drops below 10 GK, at which the neutrino-matter interactions freeze. The initial mass fractions of isotopes for the ejected trajectories are assigned assuming nuclear statistical equilibrium (NSE). The mass fractions are then evolved by solving the network following the density and temperature evolution of each trajectory individually. Beyond the hydrodynamic simulation time, we extrapolate the density and temperature of the ejecta by $\rho(t) \propto t^{-3}$ and $T(t) \propto t^{-1}$ as functions of time t to feature the free expansion of the ejected

¹ <https://stellarcollapse.org/>

² The half-life of ^{56}Ni is set to be $7.605 \times 10^5 \text{ s}$ instead (Arnett 1982).

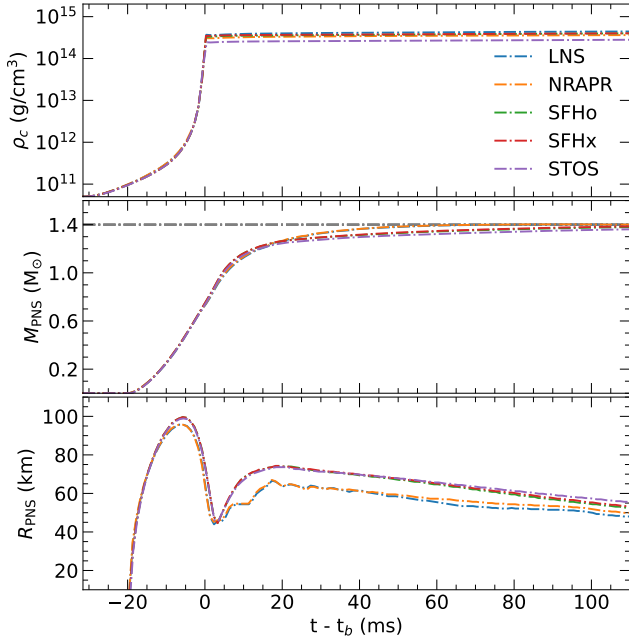


Figure 2. Time evolution of the central density ρ_c (upper panel), PNS mass M_{PNS} (middle panel), and PNS radius R_{PNS} (lower panel) for all AIC models. After the core bounce, M_{PNS} grows and approaches $1.4 M_\odot$ shown by the grey dash dotted horizontal line in the middle panel.

material. We update the network for 1 Gyr to determine the stable chemical elements produced.

3. RESULTS

3.1. Formation of proto-neutron stars

After the simulation starts, the inner region of the WD starts to collapse owing to electron capture. The core bounce (see Section 2.2) occurs at $t_b \approx 32$ ms after the start of simulation, indicating the formation of a PNS. The accretion shock induced by the core bounce propagates outward and breaks out from the WD surface at $t - t_b \approx 100 - 200$ ms (EoS dependent) after the bounce. The time evolution of the central density, mass, and radius of the PNS, defined to be the inner region of the star with density $\rho \geq 10^{11}$ g cm⁻³, are shown in Figure 2 for the SFHo model. After the core bounce, the PNS accretes surrounding matter and contracts in size. The accretion by the PNS is insensitive to the EoS, and the resulting PNS through AIC always grows to $M_{\text{PNS}} \approx 1.4 M_\odot$ for all EoSs used in this work.

3.2. Neutrino signals

After the formation of a PNS, a neutronization burst of electron neutrinos is emitted. The time evolution of neutrino signals of AIC after the core bounce is shown in Figure 3 for the STOS model. The peak luminosity of the neutronization

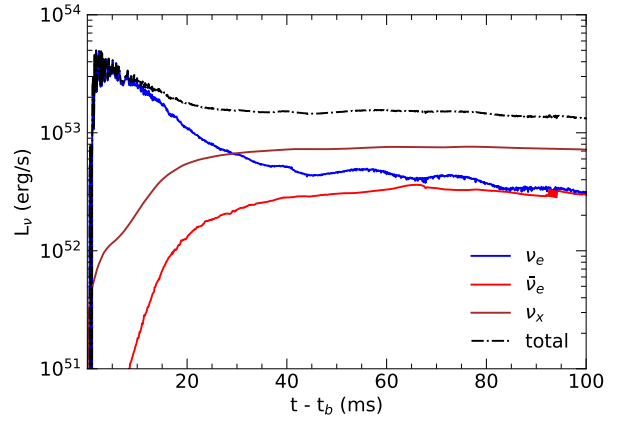


Figure 3. Time evolution of neutrino luminosity L_ν for the AIC model with the STOS EoS. The total luminosity combining all flavors is indicated by the black dashed-dotted curve.

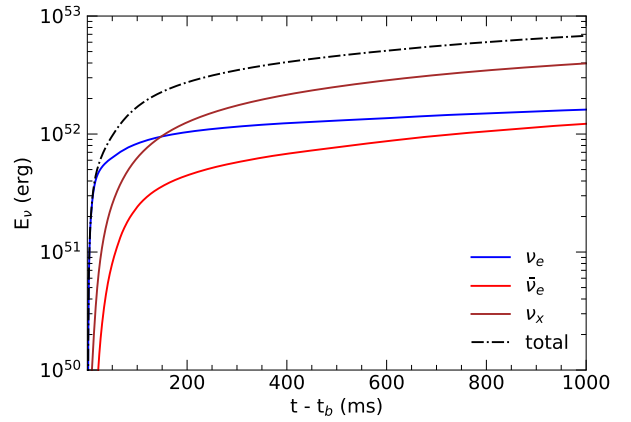


Figure 4. Cumulative energy loss through neutrino emission E_ν for the AIC model with the STOS EoS. The total energy loss combining all flavors is indicated by the black dashed-dotted curve.

burst is $\approx 5 \times 10^{53}$ erg s⁻¹. The PNS emits neutrino fluxes in all flavours subsequently, and the luminosity of each flavour remains at $\sim 10^{52}$ erg s⁻¹ until the end of the simulation. The cumulative energy released through neutrino emission for the same model is shown in Figure 4. The neutrino signals for other models are found to be quite similar to those displayed in Figure 3 and Figure 4. At the end of the simulations, the total energy released through neutrino emission is $\approx 6(7) \times 10^{52}$ erg for the models using low (intermediate and high) stiffness EoSs.

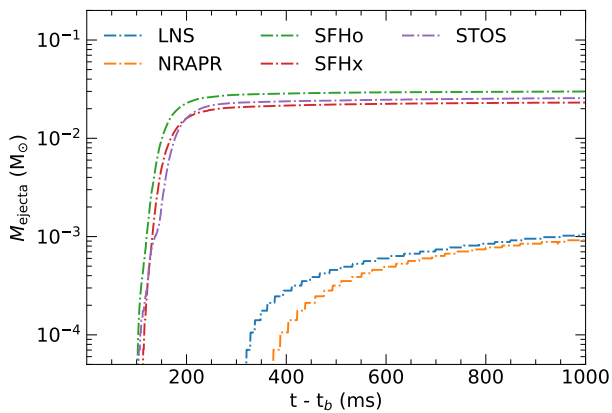
3.3. Nucleosynthesis

The envelope of the WD is expelled after the accretion shock breaks out of the star's surface. After that, a neutrino-driven wind is developed to eject the material from the surface of the star continuously. The time evolution of ejecta mass af-

Table 1. EoS properties and simulation results.

model	K	M_{TOV}	M_{ejecta}	$M(^{56}\text{Ni})$	$M(^{90}\text{Zr})$	f_{CCSN}	f_{SNIa}
LNS	211	1.72	1.02e-03	1.16e-04	2.62e-05	1.09e-01	2.72e-01
NRAPR	226	1.94	9.10e-04	4.02e-05	2.57e-05	1.11e-01	2.77e-01
SFHo	245.4	2.06	2.99e-02	3.56e-03	1.58e-04	1.81e-02	4.49e-02
SFHx	238.8	2.13	2.35e-02	4.86e-03	2.15e-04	1.33e-02	3.30e-02
STOS	281	2.23	2.60e-02	4.82e-03	6.41e-05	4.46e-02	1.11e-01

NOTE—Incompressibility K (MeV) and TOV limit M_{TOV} (M_{\odot}), the maximum mass of neutron stars, for different EoS models. The total ejecta mass M_{ejecta} , yield of ^{56}Fe , and yield of ^{90}Zr for these models are shown in units of M_{\odot} . The event rate of AIC relative to those of CCSNe f_{CCSN} and Type Ia SNe f_{SNIa} are evaluated using Equation (7) and Equation (8), respectively.

**Figure 5.** Time evolution of the total ejecta mass for all models.

ter the core bounce in different models is displayed in Figure 5. The mass outflow properties, especially the ejecta mass, are sensitive to the EoS chosen in different models. The ejecta mass is generally larger when an EoS with higher stiffness is adopted. At the end of hydrodynamic simulations, the ejecta mass of AIC is $\sim 10^{-3}(10^{-2}) M_{\odot}$ for the models using low (intermediate and high) stiffness EoSs. We map the temperature, density, and electron fraction of the ejecta to about 30 trajectories with a conserved enclosed mass throughout the simulations. The ejected trajectories from the LNS and SFHx models are displayed in Figure 6 to illustrate the EoS stiffness dependence of the ejecta properties.

We start the nucleosynthesis calculations when the temperature of an ejected trajectory drops below 10 GK, and the NSE is assumed to determine the initial mass fraction of each isotope. The initial compositions are predominantly neutrons, protons, and alpha particles. The initial neutron excess is then quantified by the electron fraction Y_e . For the SFHo, SFHx, and STOS models, the outermost few ejected trajectories never exceed 10 GK throughout the simulations (see

the upper panel in Figure 7(b) for the SFHx model as an example). We start the nucleosynthesis calculations for these few trajectories after the highest temperatures ($\gtrsim 5$ GK) are reached.

The mass fractions of ^4He , ^{56}Fe , ^{88}Sr , ^{89}Y , and ^{90}Zr versus the mass coordinate M_{coord} of the ejected trajectories in the end of the nucleosynthesis calculations are displayed in the upper panel of Figure 7 for the LNS and SFHx models. The synthesis of heavy isotopes in the AIC ejecta is mainly contributed by the (n, γ) and (α, γ) processes. For the high initial Y_e ejecta, a significant amount of ^{56}Ni (which decays to form ^{56}Fe eventually) is produced through a series of (α, γ) processes. After the freezeout of thermonuclear reactions, the proton-rich isotopes synthesized near the iron peak undergo weak decays to form stable isotopes, resulting in the drop in the final Y_e (see the lower panel of Figure 7). For the ejected trajectories with initial Y_e significantly lower than 0.5, the yield of ^{56}Ni is drastically reduced. Owing to the relatively large initial neutron excess, stable neutron-rich isotopes of Ni (e.g., ^{58}Ni and ^{60}Ni) are primarily produced. In addition, the first neutron-capture peak elements (Sr, Y, and Zr) are abundantly synthesized through the r -process in these trajectories. Unlike the high initial Y_e ejecta, the resulting isotopes produced in the low initial Y_e ejecta are mostly stable, and the initial Y_e can be retained throughout the nucleosynthesis calculation. The overall yield of ^{56}Ni , the major radioactive isotope that powers a supernova light curve, is $\sim 10^{-4}(10^{-3}) M_{\odot}$ for the models using low (intermediate and high) stiffness EoSs. Therefore, the EM light curve of AIC is at least 2 orders dimmer than those of Type Ia SNe, with a canonical yield of ^{56}Ni being about $0.63 M_{\odot}$ (Kobayashi et al. 2020b).

To compare the production curve of AIC ejecta with the solar abundances, we plot the mass fractions X of isotopes and elements relative to the solar abundances X_{\odot} (Lodders 2019) for all models in Figure 8. The elements between the

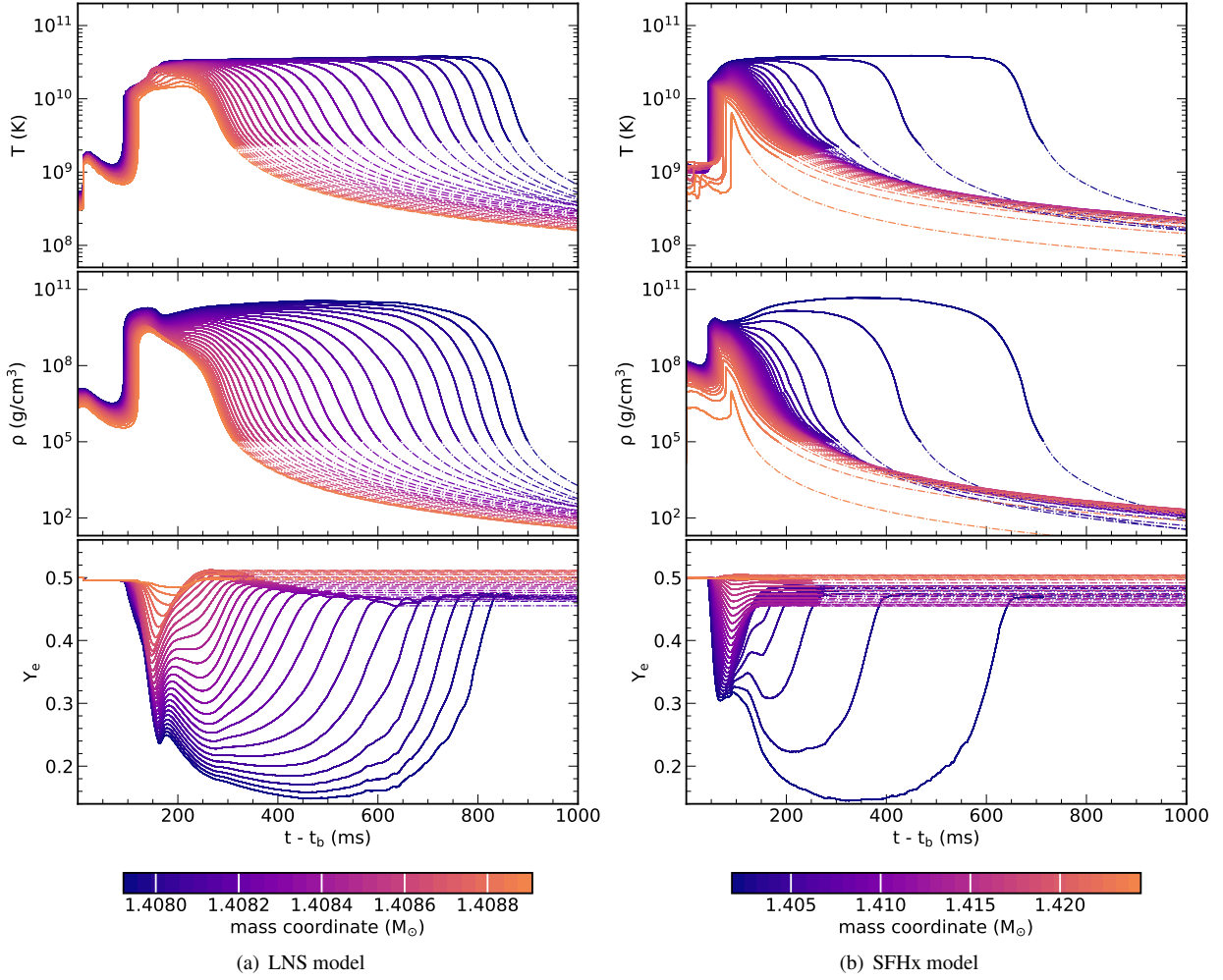


Figure 6. Time evolution of temperature T (upper panel), density ρ (middle panel), and electron fraction Y_e (lower panel) of the ejected trajectories, for two EoS models: a) LNS, b) SFHx. The trajectories are plotted in dashed-dotted lines after extrapolation starts.

iron peak and the first neutron-capture peak are abundantly synthesized. We notice that Sr, Y, and Zr are significantly overproduced with $X/X_\odot \sim 10^6$. The overproduction of even- Z elements is, in general, more significant than those of odd- Z elements. The yield of isotopes beyond Mo is negligible. The yield of isotopes for all models is shown in Appendix A.

3.4. Constraint on event rate

In this section, we follow Wanajo et al. (2009) to constrain the event rate of AICs from its chemical elements production. We firstly assume that all ^{90}Zr in nature are synthesized through AIC. The CCSNe from the progenitors heavier than $10 M_\odot$ produce $M_{\text{CCSN}}(^{16}\text{O}) = 1.5 M_\odot$ of ^{16}O per event, and the production of ^{16}O through AIC is negligible. Let the event rate of AICs relative to that of CCSNe be f_{CCSN} . We have the relation

$$f_{\text{CCSN}} = \frac{X_\odot(^{90}\text{Zr})/X_\odot(^{16}\text{O})}{M_{\text{AIC}}(^{90}\text{Zr})/M_{\text{CCSN}}(^{16}\text{O})}, \quad (7)$$

where $X_\odot(^{90}\text{Zr}) = 1.414 \times 10^{-8}$ and $X_\odot(^{16}\text{O}) = 7.422 \times 10^{-3}$ are the solar abundances of ^{90}Zr and ^{16}O , respectively (Lodders 2019).

The representative isotope produced through Type Ia SNe, on the other hand, is ^{56}Fe from the weak decay of ^{56}Ni . Analogous to Equation (7), the event rate of AICs relative to that of Type Ia SNe f_{SNIa} is given by

$$f_{\text{SNIa}} = \frac{X_\odot(^{90}\text{Zr})/X_\odot(^{56}\text{Fe})}{M_{\text{AIC}}(^{90}\text{Zr})/M_{\text{SNIa}}(^{56}\text{Fe})}, \quad (8)$$

where $X_\odot(^{56}\text{Fe}) = 1.253 \times 10^{-3}$ is the solar abundance of ^{56}Fe (Lodders 2019). We further assume that a Type Ia SN typically produces $M_{\text{SNIa}}(^{56}\text{Fe}) = 0.63 M_\odot$ of ^{56}Fe (Kobayashi et al. 2020b), and is the primary production channel of ^{56}Fe among all SNe (Dwek 2016). The numerical values of f_{CCSN} and f_{SNIa} for different models are calculated and listed in Table 1. As discussed in Section 3.3, the yield of ^{90}Zr , and hence the event rate of AIC derived, are sensitive to the initial electron fraction Y_e in the nucleosynthesis calculations. We

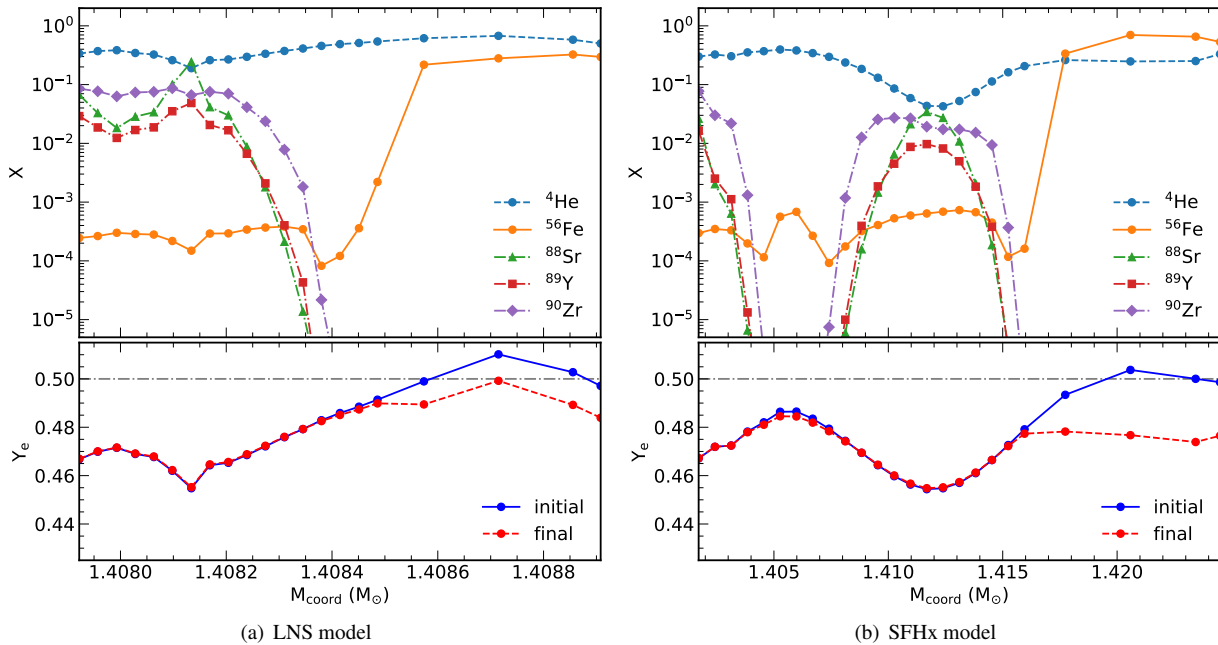


Figure 7. Upper panels: mass fractions X of a few characteristic isotopes as the end products of nucleosynthesis. Lower panels: electron fraction Y_e at the beginning (blue) and at the end (red) of nucleosynthesis calculations. The above curves are plotted vs. the mass coordinate M_{coord} of the ejected trajectories, for two EoS models: a) LNS, b) SFHx. The grey dash dotted horizontal lines in the lower panels indicate $Y_e = 0.5$ with zero neutron excess.

show in Appendix B that our results are valid up to a factor of 2 given an uncertainty of 2% in the initial Y_e of the ejecta.

4. DISCUSSIONS

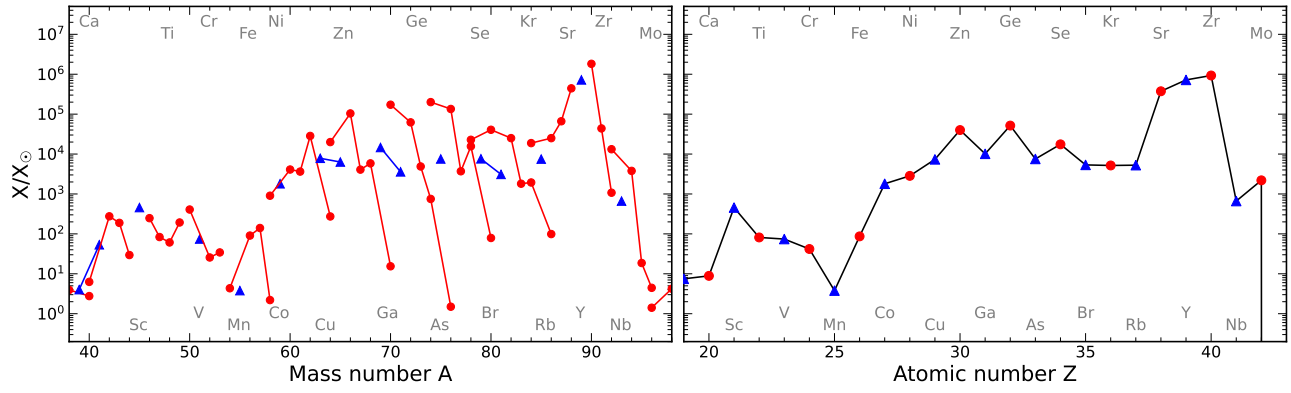
To account for the uncertainties in hot and dense nuclear matter properties, we perform the hydrodynamic simulations of AIC using five different EoSs. It is realised that the ejecta masses of AIC could differ by an order of magnitude among the EoSs presented (see Figure 5). Accordingly, the yield of heavy stable isotopes varies by an order among these models in spite of similar production curves relative to the solar abundances indicated in Figure 8. In general, the ejecta mass and yield of heavy stable isotopes are larger when a stiffer EoS is used. Hence, the constraints on AIC event rate relative to other supernovae derived in Section 3.4 are also EoS dependent. From our nucleosynthesis calculations, the upper bound of AIC event rate is $\sim 1 - 10\%$ relative to the Type Ia SN event rate, and the lower end of such results are consistent with estimations by previous studies (Darbha et al. 2010; Wang 2018).

We assume that AIC contributes to galactic chemical evolution, and is the major source of the first neutron-capture peak elements. As already pointed out in Section 1.2, nevertheless, these elements could be abundantly synthesized through ECSNe as well. The production curves of AIC we obtained are similar to those of ECSNe presented in Wanajo et al. (2009). Consequently, there is a degeneracy in the contribution to the solar abundances of these elements from both types of su-

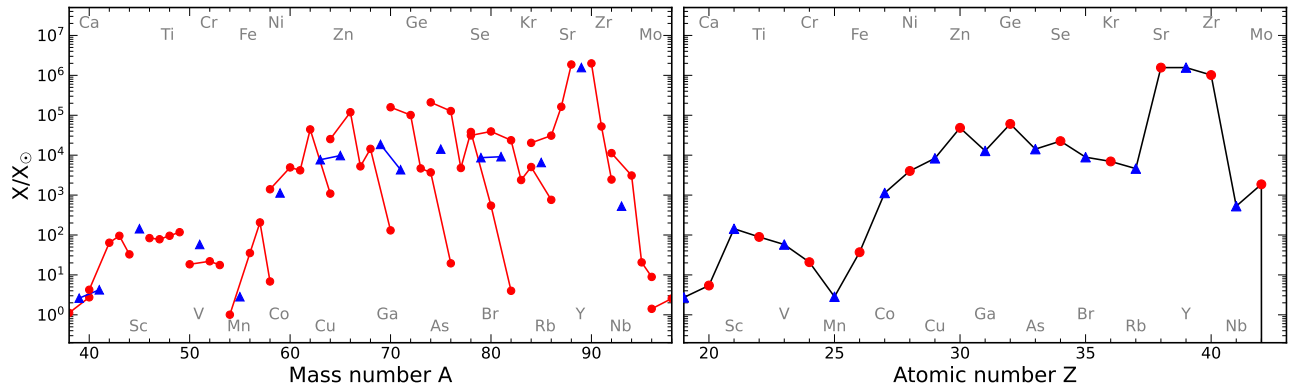
pernova. The ratios of AIC to other supernovae event rates suggested in Section 3.4 are, therefore, conservative upper bounds of its occurrence. Further effort is needed to break the degeneracy between AIC and ECSNe.

AIC could be well distinguished from standard Type Ia SNe from the associated bright neutrino signals. With faint EM signals, AIC could be further distinguished from typical CC-SNe with characteristic light curves despite similar neutrino signals. Additional efforts are required to distinguish AIC and ECSNe. For instance, radiative transfer calculations may reveal the differences in EM light curve of AIC and ECSNe with an optically thick outer envelope. After ECSN explosions, the shock heats the outer envelope, which additional powers the EM light curve of ECSNe. The compact remnants of AIC may also be distinguishable from those formed by ECSNe based on the huge difference in their progenitor masses. Meanwhile, massive highly magnetized rotating WDs are proposed as soft gamma ray repeaters and anomalous X-ray pulsars (Malheiro et al. 2012). The AIC progenitors may, therefore, be identified through EM observations before the gravitational collapse if they are highly magnetized and rapidly rotating.

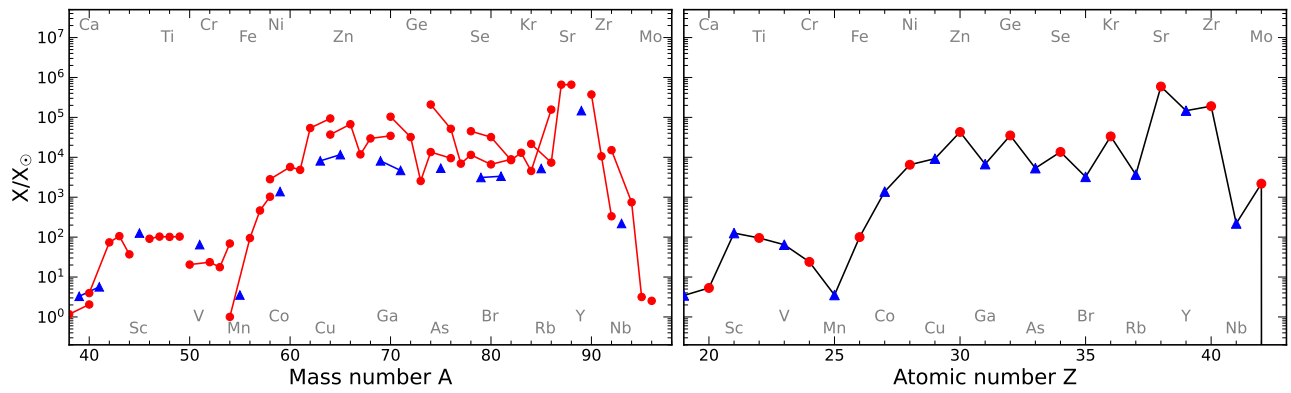
The multi-dimensional effects of the explosion dynamics and ejecta properties are not investigated in this work. It is expected that WDs are rapidly rotating because of angular momentum transfer during mass accretion. A super-Chandrasekhar WD being rotationally supported may be formed as the AIC progenitor, and the explosion dynamics of such an object may be different from our models. An



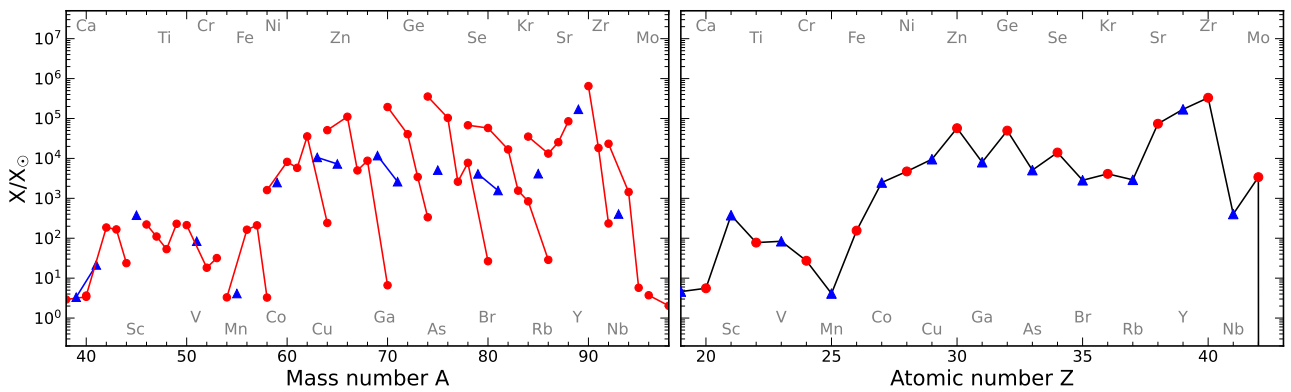
(a) LNS model



(b) NRAPR model



(c) SFHo model



(d) SFHx model

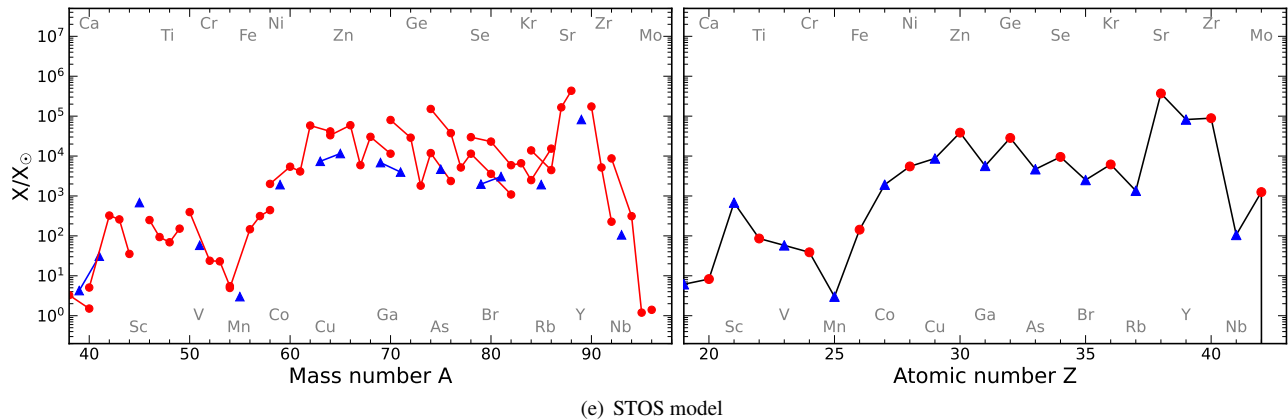


Figure 8. Mass fractions X of isotopes (left panel) and elements (right panel) over the solar abundances X_{\odot} (Lodders 2019) in the end of nucleosynthesis calculations for all models. The isotopes with the same atomic number in the left panel are connected by lines. The odd- Z (even- Z) elements are indicated by blue triangle (red circle) markers. Only the overproduced isotopes and elements ($X/X_{\odot} > 1$) are displaced.

accretion disk formed after the AIC of a rapidly rotating progenitor (see Metzger et al. 2009) is also neglected in our nucleosynthesis calculations. Apart from rotation, convection is also another significant multi-dimensional effect on AIC. The post-bounce convective flow may noticeably modify the electron fraction of the ejecta, and hence gives rise to distinct end products of nucleosynthesis. Moreover, the presence of a magnetic field is a potentially important factor to be considered in multi-dimensional magnetohydrodynamic simulations. The collapse of a WD may be delayed by magnetic pressure before core bounce. In addition, a relativistic jet may be launched after a PNS with a very strong magnetic field is formed. The overall production curve may be affected by the nucleosynthesis in the ejecta along the jet as suggested by Bhattacharya et al. (2022).

The population of AIC progenitors, namely oxygen-neon-magnesium WDs, among all WDs remains unclear. Self-consistent stellar evolution simulations are required to precisely determine whether the degenerate oxygen-neon-magnesium core of a super-AGB star would collapse without leaving a WD behind. Such simulations could also reveal the chemical composition, especially Ne and Mg that are responsible for electron capture, of the WDs formed after the super-AGB stage. Furthermore, the fate of oxygen-neon-magnesium WDs evolving towards the Chandrasekhar limit through mass accretion remains unclear. For example, Schwab et al. (2015) discussed the possibility of thermonuclear explosion of WDs after mass accretion. The later work by Kirsebom et al. (2019) showed that the thermonuclear runaway of oxygen is enhanced if the second-forbidden electron capture on neon and fluorine are included, and the WDs are

partially disrupted by the oxygen deflagration waves. These works indicate that more accurate nuclear reaction rate calculations are required to determine whether the WDs will eventually collapse or undergo a thermonuclear explosion.

5. CONCLUSIONS

We perform hydrodynamic simulations of AIC coupled with a neutrino transport scheme using various EoSs with different stiffness, and we investigate the yield of chemical elements in the supernova ejecta by post-processing nucleosynthesis calculations. We find that the ejecta mass and yield of heavy elements are sensitive to the stiffness of EoSs, while the trend of production curves is universal. The first neutron-capture peak elements could be overproduced by $\sim 10^6$ relative to the solar abundances. From the yield of ^{90}Zr , we infer that the AIC event rate cannot exceed $\sim 10\%$ of the CC-SNe and Type Ia SNe event rates to be consistent with solar abundances observation.

6. ACKNOWLEDGEMENT

We thank Ken’ichi Nomoto and Shuai Zha for the helpful discussions. We acknowledge F. X. Timmes for making the Torch nuclear reaction network calculation code open-source and the explanation about its usage. We thank P. Möller for providing the publicly available isotope weak decay rates table.

This work is partially supported by grants from the Research Grant Council of the Hong Kong Special Administrative Region, China (Project Nos. 14300320 and 14304322). This material is based upon work supported by the National Science Foundation under Grant AST-2316807.

APPENDIX

A. YIELD OF STABLE ISOTOPES

The yield of stable isotopes of the LNS, NRAPR, SFHo, SFHx, and STOS models are tabulated below.

B. SENSITIVITY TO VARIATION IN ELECTRON FRACTION

The production curve of AIC, especially the first neutron-capture peak elements, is sensitive to the initial electron frac-

Table 2. Yield of stable isotopes in units of M_{\odot} .

isotope	LNS	NRAPR	SFHo	SFHx	STOS	isotope	LNS	NRAPR	SFHo	SFHx	STOS
¹ H	4.19e-06	4.96e-10	1.59e-11	2.24e-05	1.03e-04	⁵⁹ Co	6.81e-06	3.83e-06	1.54e-04	2.17e-04	1.86e-04
⁴ He	4.78e-04	3.17e-04	5.18e-03	5.35e-03	5.75e-03	⁵⁸ Ni	4.93e-05	6.83e-05	4.52e-03	2.03e-03	2.80e-03
¹² C	6.52e-08	6.50e-08	1.75e-06	1.40e-06	9.33e-07	⁶⁰ Ni	8.92e-05	9.64e-05	3.66e-03	4.13e-03	3.02e-03
¹⁶ O	7.55e-09	2.26e-09	8.38e-09	5.65e-08	1.26e-07	⁶¹ Ni	3.49e-06	3.59e-06	1.37e-04	1.29e-04	1.01e-04
¹⁷ O	2.77e-10	3.46e-14	6.85e-17	1.74e-09	7.21e-09	⁶² Ni	8.85e-05	1.23e-04	4.95e-03	2.57e-03	4.65e-03
¹⁸ O	1.72e-11	3.26e-18	0.00e+00	1.04e-10	7.82e-10	⁶⁴ Ni	2.23e-07	7.97e-07	2.26e-03	4.56e-06	8.70e-04
²⁰ Ne	1.22e-09	1.77e-09	1.13e-08	1.74e-08	2.16e-08	⁶³ Cu	5.18e-06	4.56e-06	1.58e-04	1.62e-04	1.25e-04
²¹ Ne	1.99e-11	8.37e-12	4.34e-14	1.14e-10	5.11e-10	⁶⁵ Cu	1.92e-06	2.66e-06	1.04e-04	5.11e-05	9.02e-05
²² Ne	5.34e-09	1.93e-12	1.03e-17	3.51e-08	9.26e-08	⁶⁴ Zn	2.25e-05	2.55e-05	1.23e-03	1.33e-03	9.58e-04
²³ Na	1.57e-10	2.79e-14	3.66e-13	1.50e-09	3.35e-09	⁶⁶ Zn	6.81e-05	6.98e-05	1.30e-03	1.67e-03	9.94e-04
²⁴ Mg	6.69e-10	1.32e-09	1.65e-08	1.57e-08	8.36e-09	⁶⁷ Zn	3.95e-07	4.55e-07	3.37e-05	1.12e-05	1.47e-05
²⁵ Mg	2.76e-10	5.92e-10	6.00e-12	7.00e-10	3.72e-09	⁶⁸ Zn	2.63e-06	5.80e-06	3.93e-04	9.10e-05	3.49e-04
²⁶ Mg	1.09e-08	8.47e-11	1.14e-11	7.69e-08	1.63e-07	⁷⁰ Zn	2.45e-10	1.86e-09	1.61e-05	2.44e-09	4.67e-06
²⁷ Al	6.86e-09	6.70e-11	1.26e-09	4.78e-08	1.51e-07	⁶⁹ Ga	6.20e-07	7.08e-07	1.02e-05	1.15e-05	7.46e-06
²⁸ Si	6.43e-09	1.06e-08	1.29e-07	1.09e-07	9.83e-08	⁷¹ Ga	1.04e-07	1.12e-07	4.00e-06	1.75e-06	2.95e-06
²⁹ Si	1.76e-09	4.28e-10	3.32e-10	8.08e-09	4.86e-08	⁷⁰ Ge	8.45e-06	6.98e-06	1.50e-04	2.20e-04	1.01e-04
³⁰ Si	4.78e-08	9.22e-10	2.30e-08	3.82e-07	8.62e-07	⁷² Ge	4.20e-06	6.12e-06	6.36e-05	6.31e-05	5.00e-05
³¹ P	3.27e-09	9.54e-10	2.78e-08	4.63e-08	6.49e-08	⁷³ Ge	9.40e-08	8.04e-08	1.45e-06	1.53e-06	8.95e-07
³² S	1.25e-08	2.38e-08	3.82e-07	2.57e-07	1.85e-07	⁷⁴ Ge	6.92e-08	3.06e-07	3.67e-05	7.15e-07	2.81e-05
³³ S	4.15e-09	2.03e-09	6.96e-09	1.60e-08	5.46e-08	⁷⁶ Ge	3.00e-11	3.51e-10	5.62e-06	1.65e-10	1.22e-06
³⁴ S	8.55e-08	5.73e-09	1.72e-07	9.17e-07	1.68e-06	⁷⁵ As	9.73e-08	1.64e-07	2.03e-06	1.52e-06	1.55e-06
³⁵ Cl	1.01e-08	4.27e-09	1.54e-07	1.64e-07	2.16e-07	⁷⁴ Se	2.44e-07	2.30e-07	7.51e-06	1.00e-05	4.73e-06
³⁷ Cl	3.13e-09	5.94e-10	1.55e-08	5.07e-08	9.30e-08	⁷⁶ Se	1.81e-06	1.53e-06	2.05e-05	3.22e-05	1.30e-05
³⁶ Ar	1.51e-08	2.29e-08	4.20e-07	2.46e-07	3.26e-07	⁷⁷ Se	4.15e-08	4.79e-08	2.29e-06	6.77e-07	1.49e-06
³⁸ Ar	6.49e-08	1.65e-08	5.67e-07	1.11e-06	1.39e-06	⁷⁸ Se	5.54e-07	1.21e-06	1.20e-05	6.36e-06	1.04e-05
⁴⁰ Ar	1.25e-11	1.12e-11	2.74e-10	3.58e-10	1.76e-10	⁸⁰ Se	6.03e-09	3.72e-08	1.49e-05	4.70e-08	7.03e-06
³⁹ K	1.49e-08	8.72e-09	3.60e-07	2.87e-07	4.06e-07	⁸² Se	3.13e-12	4.97e-11	3.63e-06	1.23e-11	3.87e-07
⁴¹ K	1.51e-08	1.07e-09	4.72e-08	1.40e-07	2.24e-07	⁷⁹ Br	1.07e-07	1.09e-07	1.29e-06	1.33e-06	7.12e-07
⁴⁰ Ca	3.95e-07	2.40e-07	7.34e-06	5.34e-06	8.21e-06	⁸¹ Br	4.33e-08	1.15e-07	1.38e-06	5.08e-07	1.10e-06
⁴² Ca	1.21e-07	2.53e-08	9.59e-07	1.90e-06	3.66e-06	⁷⁸ Kr	9.57e-09	1.18e-08	5.57e-07	6.59e-07	3.21e-07
⁴³ Ca	1.77e-08	8.04e-09	2.93e-07	3.62e-07	6.24e-07	⁸⁰ Kr	1.10e-07	9.59e-08	2.57e-06	3.64e-06	1.61e-06
⁴⁴ Ca	4.40e-08	4.37e-08	1.62e-06	8.21e-07	1.35e-06	⁸² Kr	3.49e-07	2.96e-07	3.48e-06	5.41e-06	2.11e-06
⁴⁵ Sc	1.96e-08	5.52e-09	1.60e-07	3.75e-07	7.52e-07	⁸³ Kr	2.53e-08	2.99e-08	5.36e-06	5.04e-07	2.37e-06
⁴⁶ Ti	6.56e-08	1.98e-08	7.10e-07	1.36e-06	1.69e-06	⁸⁴ Kr	1.35e-07	3.15e-07	9.31e-06	1.36e-06	4.45e-06
⁴⁷ Ti	2.03e-08	1.71e-08	7.40e-07	6.24e-07	5.85e-07	⁸⁶ Kr	2.12e-09	1.46e-08	9.90e-05	1.43e-08	8.44e-06
⁴⁸ Ti	1.50e-07	2.11e-07	7.36e-06	3.04e-06	4.37e-06	⁸⁵ Rb	9.16e-08	7.19e-08	1.89e-06	1.17e-06	6.04e-07
⁴⁹ Ti	3.57e-08	1.95e-08	5.62e-07	9.85e-07	7.21e-07	⁸⁴ Sr	5.83e-09	5.65e-09	1.97e-07	2.52e-07	1.10e-07
⁵⁰ Ti	2.68e-12	4.38e-12	2.06e-09	1.36e-11	2.59e-11	⁸⁶ Sr	1.40e-07	1.55e-07	1.22e-06	1.72e-06	6.42e-07
⁵¹ V	2.95e-08	2.06e-08	7.57e-07	7.73e-07	5.91e-07	⁸⁷ Sr	2.64e-07	5.81e-07	7.72e-05	2.34e-06	1.69e-05
⁵⁰ Cr	3.30e-07	1.34e-08	4.89e-07	3.99e-06	8.21e-06	⁸⁸ Sr	2.12e-05	8.03e-05	9.32e-04	9.45e-05	5.32e-04
⁵² Cr	4.16e-07	3.19e-07	1.13e-05	6.86e-06	9.92e-06	⁸⁹ Y	7.91e-06	1.54e-05	4.76e-05	4.32e-05	2.32e-05
⁵³ Cr	6.45e-08	2.98e-08	9.76e-07	1.38e-06	1.11e-06	⁹⁰ Zr	2.62e-05	2.57e-05	1.58e-04	2.15e-04	6.41e-05
⁵⁴ Cr	1.49e-10	1.46e-10	9.67e-07	9.91e-10	6.70e-08	⁹¹ Zr	1.39e-07	1.49e-07	9.88e-07	1.34e-06	4.21e-07
⁵⁵ Mn	5.37e-08	3.61e-08	1.48e-06	1.35e-06	1.09e-06	⁹² Zr	5.26e-09	1.07e-08	4.79e-08	2.66e-08	2.84e-08
⁵⁴ Fe	3.39e-07	7.05e-08	2.31e-06	5.97e-06	9.94e-06	⁹³ Nb	1.37e-09	9.73e-10	1.33e-08	1.92e-08	5.59e-09
⁵⁶ Fe	1.15e-04	4.03e-05	3.55e-03	4.82e-03	4.79e-03	⁹² Mo	1.31e-08	1.00e-08	4.41e-07	5.34e-07	2.22e-07
⁵⁷ Fe	4.20e-06	5.54e-06	4.09e-04	1.46e-04	2.41e-04	⁹⁴ Mo	2.40e-09	1.76e-09	1.39e-08	2.12e-08	5.08e-09
⁵⁸ Fe	8.89e-09	2.49e-08	1.23e-04	3.06e-07	4.59e-05	⁹⁵ Mo	2.07e-11	2.05e-11	1.03e-10	1.48e-10	3.40e-11

tion Y_e of the ejecta, as the yield of neutron-rich isotopes is directly related to the initial neutron excess. In realistic supernova simulations, the Y_e of ejecta may be subject to an uncertainty up to a few percents due to both finite numerical resolution and other physical effects, such as convective mixing and uncertainties of neutrino-matter interaction rates (see the discussions in [Wanajo et al. 2009](#), for more details). Here, we study the sensitivity of nucleosynthesis yield to the initial Y_e of the ejecta to quantify the robustness of our results.

We artificially modify the initial Y_e of the ejecta by $\pm 1\%$ and $\pm 2\%$ at the beginning of nucleosynthesis calculations done in Section 3.3 for all models. We find that the yield of heavy elements, especially the first neutron-capture peak elements, is significantly altered. In general, the yield of these heavy elements increases (decreases) when the initial Y_e decreases (increases). The comparison among the production curves with different initial Y_e is shown in Figure 9 for the

LNS and SFHx models. A wide range of initial Y_e , down to $Y_e \lesssim 0.46$, is covered by the AIC ejecta in all models. We notice that the yield of ^{90}Zr peaks at $Y_e \approx 0.46$ in most of the trajectories. When we shift the initial Y_e of all trajectories downward, the overall enhancement of ^{90}Zr production is somehow compensated by the reduction of ^{90}Zr production in a few trajectories with $Y_e < 0.46$, and vice versa. The yield of ^{88}Sr (^{89}Y), on the other hand, decreases monotonically with Y_e for $Y_e \gtrsim 0.44$ (0.45). For the range of initial Y_e covered by the AIC ejecta, a downward shifting in Y_e results in a large enhancement of ^{88}Sr and ^{89}Y production in general. Hence, the yield of ^{90}Zr is less sensitive to Y_e compared to other first neutron-capture peak elements in our models. Within an uncertainty of $\pm 2\%$ for the initial Y_e , we find that the yield of ^{90}Zr may vary by a factor of 2 in all models. The event rates of AIC reported in Table 1 are, correspondingly, valid up to a factor of 2, assuming such an uncertainty of Y_e .

REFERENCES

- Abdikamalov, E. B., Ott, C. D., Rezzolla, L., et al. 2010, *PhRvD*, 81, 044012, doi: [10.1103/PhysRevD.81.044012](https://doi.org/10.1103/PhysRevD.81.044012)
- Arnett, W. D. 1982, *ApJ*, 253, 785, doi: [10.1086/159681](https://doi.org/10.1086/159681)
- Berninger, H., Frénod, E., Gander, M., Liebendörfer, M., & Michaud, J. 2013, *SIAM Journal on Mathematical Analysis*, 45, 3229, doi: [10.1137/12089243X](https://doi.org/10.1137/12089243X)
- Bhattacharya, M., Horiuchi, S., & Murase, K. 2022, *MNRAS*, 514, 6011, doi: [10.1093/mnras/stac1721](https://doi.org/10.1093/mnras/stac1721)
- Cao, L. G., Lombardo, U., Shen, C. W., & Giai, N. V. 2006, *PhRvC*, 73, 014313, doi: [10.1103/PhysRevC.73.014313](https://doi.org/10.1103/PhysRevC.73.014313)
- Chan, H.-S., Chu, M.-c., & Leung, S.-C. 2023, *ApJ*, 945, 133, doi: [10.3847/1538-4357/acbc1d](https://doi.org/10.3847/1538-4357/acbc1d)
- Cowan, J. J., Sneden, C., Lawler, J. E., et al. 2021, *Reviews of Modern Physics*, 93, 015002, doi: [10.1103/RevModPhys.93.015002](https://doi.org/10.1103/RevModPhys.93.015002)
- Cyburt, R. H., Amthor, A. M., Ferguson, R., et al. 2010, *ApJS*, 189, 240, doi: [10.1088/0067-0049/189/1/240](https://doi.org/10.1088/0067-0049/189/1/240)
- Darba, S., Metzger, B. D., Quataert, E., et al. 2010, *MNRAS*, 409, 846, doi: [10.1111/j.1365-2966.2010.17353.x](https://doi.org/10.1111/j.1365-2966.2010.17353.x)
- Dessart, L., Burrows, A., Livne, E., & Ott, C. D. 2007, *ApJ*, 669, 585, doi: [10.1086/521701](https://doi.org/10.1086/521701)
- Dessart, L., Burrows, A., Ott, C. D., et al. 2006, *ApJ*, 644, 1063, doi: [10.1086/503626](https://doi.org/10.1086/503626)
- Dwek, E. 2016, *ApJ*, 825, 136, doi: [10.3847/0004-637X/825/2/136](https://doi.org/10.3847/0004-637X/825/2/136)
- Falcone, A., & DUNE Collaboration. 2022, *Nuclear Instruments and Methods in Physics Research A*, 1041, 167217, doi: [10.1016/j.nima.2022.167217](https://doi.org/10.1016/j.nima.2022.167217)
- Farrow, N., Zhu, X.-J., & Thrane, E. 2019, *ApJ*, 876, 18, doi: [10.3847/1538-4357/ab12e3](https://doi.org/10.3847/1538-4357/ab12e3)
- Fryer, C., Benz, W., Herant, M., & Colgate, S. A. 1999, *ApJ*, 516, 892, doi: [10.1086/307119](https://doi.org/10.1086/307119)
- Hempel, M., Fischer, T., Schaffner-Bielich, J., & Liebendörfer, M. 2012, *ApJ*, 748, 70, doi: [10.1088/0004-637X/748/1/70](https://doi.org/10.1088/0004-637X/748/1/70)
- Hempel, M., & Schaffner-Bielich, J. 2010, *NuPhA*, 837, 210, doi: [10.1016/j.nuclphysa.2010.02.010](https://doi.org/10.1016/j.nuclphysa.2010.02.010)
- Itoh, N., Hayashi, H., Nishikawa, A., & Kohyama, Y. 1996, *ApJS*, 102, 411, doi: [10.1086/192264](https://doi.org/10.1086/192264)
- Kajino, T., Aoki, W., Balantekin, A. B., et al. 2019, *Progress in Particle and Nuclear Physics*, 107, 109, doi: [10.1016/j.pnpnp.2019.02.008](https://doi.org/10.1016/j.pnpnp.2019.02.008)
- Kirsebom, O. S., Jones, S., Strömberg, D. F., et al. 2019, *Phys. Rev. Lett.*, 123, 262701, doi: [10.1103/PhysRevLett.123.262701](https://doi.org/10.1103/PhysRevLett.123.262701)
- Kobayashi, C., Karakas, A. I., & Lugaro, M. 2020a, *ApJ*, 900, 179, doi: [10.3847/1538-4357/abae65](https://doi.org/10.3847/1538-4357/abae65)
- Kobayashi, C., Leung, S.-C., & Nomoto, K. 2020b, *ApJ*, 895, 138, doi: [10.3847/1538-4357/ab8e44](https://doi.org/10.3847/1538-4357/ab8e44)
- Lattimer, J. M., & Douglas Swesty, F. 1991, *Nuclear Physics A*, 535, 331, doi: [https://doi.org/10.1016/0375-9474\(91\)90452-C](https://doi.org/10.1016/0375-9474(91)90452-C)
- Leung, S. C., Chu, M. C., & Lin, L. M. 2015, *MNRAS*, 454, 1238, doi: [10.1093/mnras/stv1923](https://doi.org/10.1093/mnras/stv1923)
- Leung, S.-C., & Nomoto, K. 2019, *PASA*, 36, e006, doi: [10.1017/pasa.2018.49](https://doi.org/10.1017/pasa.2018.49)
- Leung, S.-C., Nomoto, K., & Suzuki, T. 2020, *ApJ*, 889, 34, doi: [10.3847/1538-4357/ab5d2f](https://doi.org/10.3847/1538-4357/ab5d2f)
- Leung, S.-C., Zha, S., Chu, M.-C., Lin, L.-M., & Nomoto, K. 2019, *ApJ*, 884, 9, doi: [10.3847/1538-4357/ab3b5e](https://doi.org/10.3847/1538-4357/ab3b5e)
- Liebendörfer, M. 2005, *ApJ*, 633, 1042, doi: [10.1086/466517](https://doi.org/10.1086/466517)
- Liebendörfer, M., Whitehouse, S. C., & Fischer, T. 2009, *ApJ*, 698, 1174, doi: [10.1088/0004-637X/698/2/1174](https://doi.org/10.1088/0004-637X/698/2/1174)
- Lodders, K. 2019, arXiv e-prints, arXiv:1912.00844, doi: [10.48550/arXiv.1912.00844](https://doi.org/10.48550/arXiv.1912.00844)

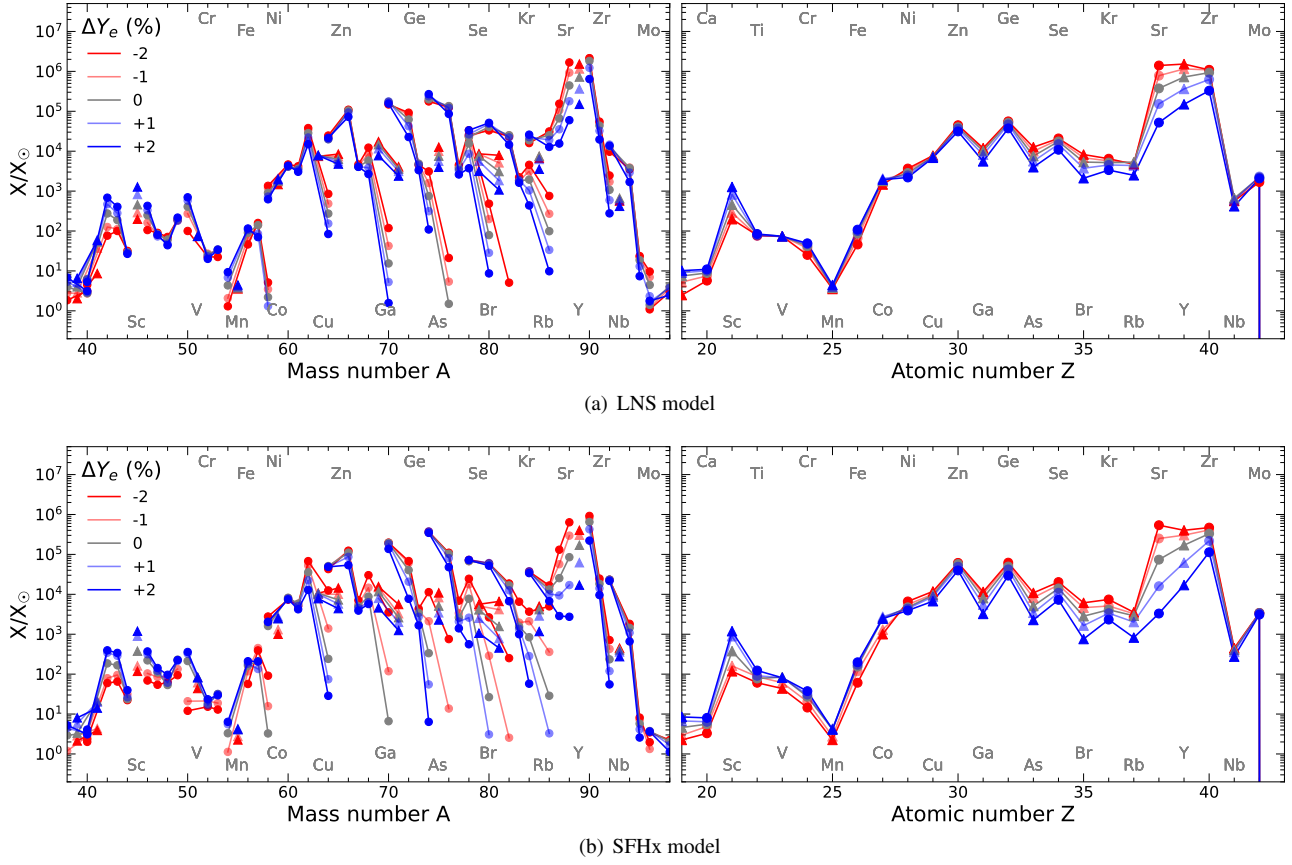


Figure 9. Same figure as Figure 8, but the production curves with initial electron fraction Y_e of ejecta artificially modified by +1 % (pale blue), +2 % (blue), -1 % (pale red), and -2 % (red) are attached to compare with the canonical production curve (grey) for two EoS models: a) LNS, b) SFHx.

- Malheiro, M., Rueda, J. A., & Ruffini, R. 2012, PASJ, 64, 56, doi: [10.1093/pasj/64.3.56](https://doi.org/10.1093/pasj/64.3.56)
- Marek, A., Dimmelmeier, H., Janka, H. T., Müller, E., & Buras, R. 2006, A&A, 445, 273, doi: [10.1051/0004-6361:20052840](https://doi.org/10.1051/0004-6361:20052840)
- Margalit, B., Berger, E., & Metzger, B. D. 2019, ApJ, 886, 110, doi: [10.3847/1538-4357/ab4c31](https://doi.org/10.3847/1538-4357/ab4c31)
- Metzger, B. D., Piro, A. L., & Quataert, E. 2009, MNRAS, 396, 1659, doi: [10.1111/j.1365-2966.2009.14909.x](https://doi.org/10.1111/j.1365-2966.2009.14909.x)
- Micchi, L. F. L., Radice, D., & Chirenti, C. 2023, MNRAS, doi: [10.1093/mnras/stad2420](https://doi.org/10.1093/mnras/stad2420)
- Möller, P., Nix, J., & Kratz, K.-L. 1997, Atomic Data and Nuclear Data Tables, 66, 131
- Möller, P., Pfeiffer, B., & Kratz, K.-L. 2003, PhRvC, 67, 055802, doi: [10.1103/PhysRevC.67.055802](https://doi.org/10.1103/PhysRevC.67.055802)
- Mori, M., Sawada, R., Suwa, Y., et al. 2023, arXiv e-prints, arXiv:2306.17381, doi: [10.48550/arXiv.2306.17381](https://doi.org/10.48550/arXiv.2306.17381)
- Moriya, T. J. 2016, ApJL, 830, L38, doi: [10.3847/2041-8205/830/2/L38](https://doi.org/10.3847/2041-8205/830/2/L38)
- Nomoto, K., & Kondo, Y. 1991, ApJL, 367, L19, doi: [10.1086/185922](https://doi.org/10.1086/185922)
- Piro, A. L., & Kulkarni, S. R. 2013, ApJL, 762, L17, doi: [10.1088/2041-8205/762/2/L17](https://doi.org/10.1088/2041-8205/762/2/L17)
- Rosswog, S., & Liebendörfer, M. 2003, MNRAS, 342, 673, doi: [10.1046/j.1365-8711.2003.06579.x](https://doi.org/10.1046/j.1365-8711.2003.06579.x)
- Ruiter, A. J., Ferrario, L., Belczynski, K., et al. 2019, MNRAS, 484, 698, doi: [10.1093/mnras/stz001](https://doi.org/10.1093/mnras/stz001)
- Schneider, A. S., Constantinou, C., Muccioli, B., & Prakash, M. 2019, Phys. Rev. C, 100, 025803, doi: [10.1103/PhysRevC.100.025803](https://doi.org/10.1103/PhysRevC.100.025803)
- Schneider, A. S., Roberts, L. F., & Ott, C. D. 2017, Phys. Rev. C, 96, 065802, doi: [10.1103/PhysRevC.96.065802](https://doi.org/10.1103/PhysRevC.96.065802)
- Schwab, J., Podsiadlowski, P., & Rappaport, S. 2010, ApJ, 719, 722, doi: [10.1088/0004-637X/719/1/722](https://doi.org/10.1088/0004-637X/719/1/722)
- Schwab, J., Quataert, E., & Bildsten, L. 2015, MNRAS, 453, 1910, doi: [10.1093/mnras/stv1804](https://doi.org/10.1093/mnras/stv1804)
- Shen, H., Toki, H., Oyamatsu, K., & Sumiyoshi, K. 1998, NuPhA, 637, 435, doi: [10.1016/S0375-9474\(98\)00236-X](https://doi.org/10.1016/S0375-9474(98)00236-X)
- . 2011, ApJS, 197, 20, doi: [10.1088/0067-0049/197/2/20](https://doi.org/10.1088/0067-0049/197/2/20)
- Skinner, M. A., Burrows, A., & Dolence, J. C. 2016, ApJ, 831, 81, doi: [10.3847/0004-637X/831/1/81](https://doi.org/10.3847/0004-637X/831/1/81)
- Steiner, A., Prakash, M., Lattimer, J., & Ellis, P. 2005, Physics Reports, 411, 325, doi: <https://doi.org/10.1016/j.physrep.2005.02.004>
- Steiner, A. W., Hempel, M., & Fischer, T. 2013, ApJ, 774, 17, doi: [10.1088/0004-637X/774/1/17](https://doi.org/10.1088/0004-637X/774/1/17)
- Timmes, F. X., Hoffman, R. D., & Woosley, S. E. 2000, ApJS, 129, 377, doi: [10.1086/313407](https://doi.org/10.1086/313407)
- Wanajo, S., Janka, H.-T., & Müller, B. 2011, ApJL, 726, L15, doi: [10.1088/2041-8205/726/2/L15](https://doi.org/10.1088/2041-8205/726/2/L15)
- Wanajo, S., Nomoto, K., Janka, H. T., Kitaura, F. S., & Müller, B. 2009, ApJ, 695, 208, doi: [10.1088/0004-637X/695/1/208](https://doi.org/10.1088/0004-637X/695/1/208)
- Wang, B. 2018, MNRAS, 481, 439, doi: [10.1093/mnras/sty2278](https://doi.org/10.1093/mnras/sty2278)
- Woosley, S. E., & Baron, E. 1992, ApJ, 391, 228, doi: [10.1086/171338](https://doi.org/10.1086/171338)
- Wu, C.-Y., & Wang, B. 2018, Research in Astronomy and Astrophysics, 18, 036, doi: [10.1088/1674-4527/18/3/36](https://doi.org/10.1088/1674-4527/18/3/36)
- Yang, Y., & JUNO Collaboration. 2022, Nuclear Instruments and Methods in Physics Research A, 1042, 167435, doi: [10.1016/j.nima.2022.167435](https://doi.org/10.1016/j.nima.2022.167435)
- Yi, I., & Blackman, E. G. 1998, ApJL, 494, L163, doi: [10.1086/311192](https://doi.org/10.1086/311192)
- Yu, Y.-W., Chen, A., & Li, X.-D. 2019, ApJL, 877, L21, doi: [10.3847/2041-8213/ab1f85](https://doi.org/10.3847/2041-8213/ab1f85)
- Zha, S., Chu, M.-C., Leung, S.-C., & Lin, L.-M. 2019, ApJ, 883, 13, doi: [10.3847/1538-4357/ab3640](https://doi.org/10.3847/1538-4357/ab3640)
- Zha, S., O'Connor, E. P., Chu, M.-c., Lin, L.-M., & Couch, S. M. 2020, PhRvL, 125, 051102, doi: [10.1103/PhysRevLett.125.051102](https://doi.org/10.1103/PhysRevLett.125.051102)